Available online at www.sciencedirect.com
ScienceDirect
Trans. Nonferrous Met. Soc. China 33(2023) 3452−3464
Transactions of Nonferrous Metals Society of China
www.tnmsc.cn

Co_9S_8/CNTs microspheres as superior-performance cathodes in aqueous ammonium-ion batteries

Yu-zhu HUANG[1,2], Lin XING[1,2], Shuang PEI[1,2], Wei ZHOU[2],
Yu-jie HU[1], Wei-na DENG[2], Liang CHEN[2], Hai ZHU[2], Han CHEN[2]

1. College of Materials and Advanced Manufacturing, Hunan University of Technology, Zhuzhou 412007, China;
2. School of Materials and Environmental Engineering, Changsha University, Changsha 410022, China

Received 14 June 2023; accepted 8 October 2023

Abstract: Coated Co_9S_8/carbon nanotube (Co_9S_8/2CNTs) microspheres were constructed and successfully applied to aqueous ammonium-ion batteries. The introduction of carbon nanotubes in the Co_9S_8 microspheres increased the electronic conductivity, shortened the diffusion distance for NH_4^+ ions and improved the buffering ability against volume changes in the cycling processes. As a result, Co_9S_8/2CNTs microspheres had a reversible capacity of 112 mA·h/g at 0.1 A/g. In addition, the ammonium ion energy storage mechanism accompanied by the formation of reversible phase transition product $CoSO_4·6H_2O$ and establishment/breaking of intermolecular hydrogen bonds in Co_9S_8/2CNTs was investigated.

Key words: cobalt sulfide; carbon nanotubes; ammonium-ion batteries; composite microspheres; hydrogen bond

1 Introduction

Aqueous rechargeable batteries have great potential in large-scale energy storage applications due to their high safety, fast ionic conductivity, low cost and environmental friendliness. Since DAHN et al designed the first aqueous lithium-ion battery in 1994, numerous metal ions, such as K^+ [1], Na^+ [2], Zn^{2+} [3,4], Mg^{2+} [5], Ca^{2+} [6] and Al^{3+} [7], have been widely investigated as charge carriers. In recent years, aqueous nonmetal ion batteries [8] such as NH_4^+ [9], H^+ [10] and H_3O^+ [11] have received increasing attention. Compared with metallic charge carriers, nonmetallic charge carriers are irreplaceable, especially when their almost infinite resources are given. Among nonmetal cations, NH_4^+ ions as charge carriers have revealed more prominent attractions in less corrosive and lower hydrogen evolution, ultrafast ion diffusion kinetics in aqueous electrolytes and sustainable developments for safety, abundant resources and low cost in the energy storage fields [12,13]. It is worth noting that Li^+, Na^+, and K^+ are monoatomic spherical ions with a nonpreferential orientation, while NH_4^+ ions are tetrahedral polyatomic ions [14]. Different intercalation chemistry from monoatomic spherical ions and tetrahedral polyatomic ions could bring about unique topological chemistry or ionic diffusion mechanisms.

Since the pioneering attempt of WESSELLS et al [15] on the Prussian blue [16] analog $KM[Fe(CN)_6]$ (M=Cu and Ni), various electrode materials, such as conducting the polymers (polyaniline [17], PTMA [18]) and metal oxides (V_2O_5 [19], MnO_x [20], titanic acid [21], $NH_4V_4O_{10}$ [22], MoO_3 [23], WO_3 [24]), have been used for NH_4^+ storage. For example, DONG et al [19]

Corresponding author: Yu-jie HU, Tel: +86-15307335850, E-mail: hyj8622@126.com;
Han CHEN, Tel: +86-13786350206, E-mail: lzdxnchh@126.com
DOI: 10.1016/S1003-6326(23)66346-0

reported that V_2O_5 could act as an NH_4^+ host through H-bonds. The hydrogen bonding chemistry was investigated by comparing the electrochemical behavior of NH_4^+ and K^+ in the V_2O_5 host. Recently, SONG et al [20] reported the electrochemical deposition of manganese oxide (MnO_x) for NH_4^+ storage. Systematic experimental evidence and computational studies have shown the continuous building/breaking of hydrogen bonds between NH_4^+ and MnO_x layers.

The metal sulfides exhibited extraordinary potential in electrochemical energy storage fields but were hardly involved in aqueous ammonium-ion energy storage. Co_9S_8 has gained considerable attention in electrochemistry fields due to its inherent mixed valences and metallic behavior. However, Co_9S_8 exhibited poor cycling stability and rate performance owing to the volume change and dissolution of active materials during the charge and discharge processes. The combinations of Co_9S_8 and carbon-based materials were considered a promising solution [25]. The introduction of carbonaceous materials could effectively increase the electrical conductivity, alleviate the volume expansion and inhibit the dissolution of active materials during the charge and discharge processes [26,27]. Carbon nanotubes (CNTs) are promising nanocarbon materials with excellent electrical conductivity, large specific surface area, chemical stability and excellent mechanical flexibility that can modify Co_9S_8 particles [28,29]. In particular, Co_9S_8 coupled with carbon nanotubes as a cathode material for ammonium ion batteries has rarely been reported.

Herein, coated Co_9S_8/carbon nanotube (Co_9S_8/2CNT) microspheres were constructed and successfully applied in aqueous ammonium-ion batteries. The Co_9S_8/2CNTs microspheres exhibited a high capacity, excellent cycling stability and good rate performance. Some Co_9S_8 in Co_9S_8/2CNTs microspheres underwent reversible phase transformation to form $CoSO_4·6H_2O$ during the charge/discharge processes, while the reaction kinetics of the electrodes, including the evolution of the first-cycle transport kinetics, was further investigated to demonstrate the pseudocapacitive properties of NH_4^+ embedding/de-embedding behavior in Co_9S_8/2CNTs microspheres, and the diffusion process was always accompanied by uninterrupted intermolecular hydrogen bond building/breaking. This investigation provided a promising strategy for aqueous ammonium-ion storage.

2 Experimental

2.1 Synthesis of Co_9S_8

Co_9S_8 was prepared by solvothermal method. 4.3572 g cobalt acetate tetrahydrate and 1.3332 g thiourea were dissolved in 100 mL ethylene glycol and stirred under magnetic stirrers for 30 min. The uniform solution was transferred to a 100 mL Teflon lined stainless steel reactor for hydrothermal reaction at 200 °C for 48 h. The product was collected by centrifugation at a speed of 6000 r/min for 20 min, washed with ethanol and deionized water for several times, and dried in a vacuum drying oven at 60 °C for 3 h.

2.2 Synthesis of Co_9S_8/2CNTs

2 wt.% CNTs coated Co_9S_8 (Co_9S_8/2CNTs) was prepared by solvothermal method. 0.5 g Co_9S_8 and 0.1 g CNTs were dispersed in 100 mL ethylene glycol (the control group was 0.5 g Co_9S_8 dispersed in 100 mL ethylene glycol), stirred under magnetic stirrers for 30 min, and the homogeneous solution was transferred to a 100 mL PTFE-lined stainless steel reactor for hydrothermal reaction. The reaction temperature was 200 °C, and the reaction time was 24 h. The obtained product was centrifuged at 6000 r/min for 20 min, washed with ethanol and deionized water for several times, and dried in a vacuum drying oven at 60 °C for 3 h.

3 Results and discussion

3.1 Phase structure and chemical component analysis

Figure 1(a) shows the XRD patterns of the Co_9S_8 and Co_9S_8/2CNTs microspheres. The diffraction peaks of the two microspheres were attributed to cubic Co_9S_8 phase (PDF# 65-1765). The CNT diffraction peaks were invisibly observed in the Co_9S_8/2CNT microspheres due to the low CNT content. Nevertheless, the presence of CNTs could be confirmed by Raman spectra (Fig. 1(b)). The two obvious peaks positioned at 1333 and 1589 cm^{-1} could be assigned to the D-band induced by disordered carbon and the G-band related to graphitized carbon, respectively. The ratio of the

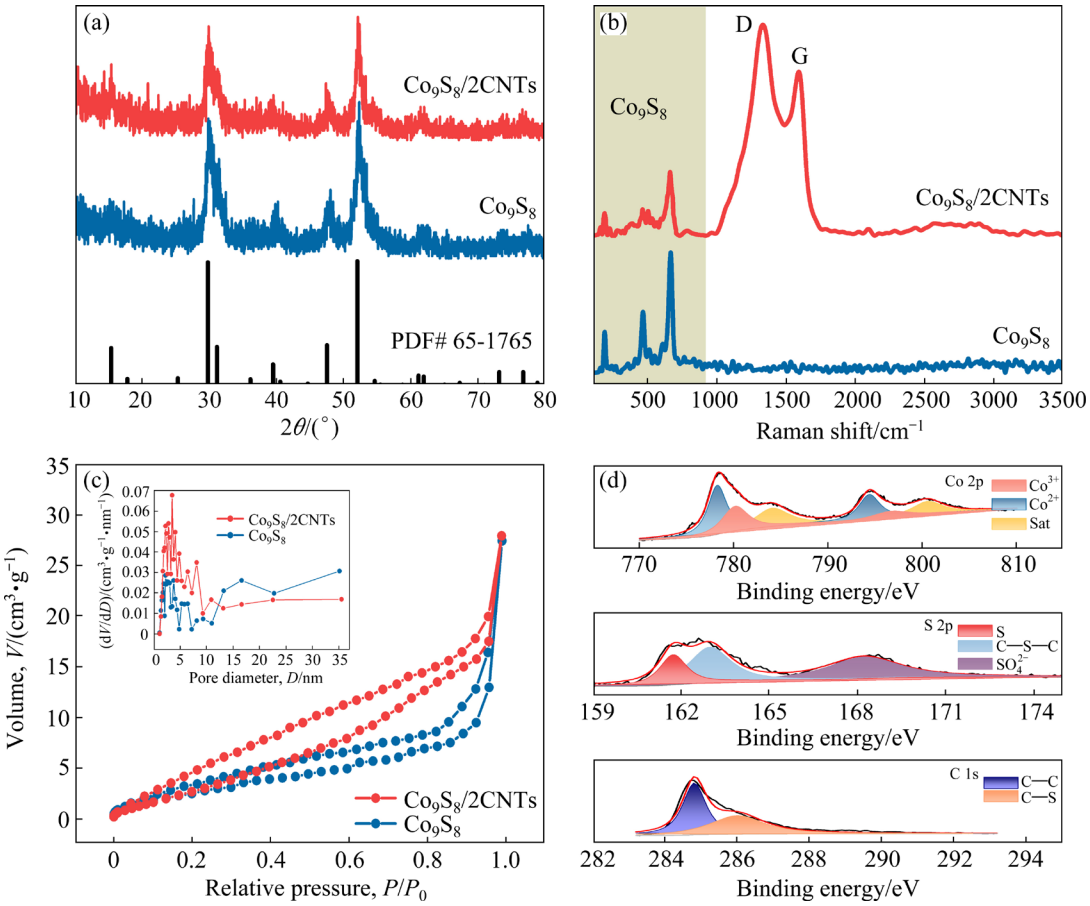

Fig. 1 XRD patterns (a), Raman spectra (b) and nitrogen adsorption−desorption isotherms (c) of Co_9S_8 and Co_9S_8/2CNTs, and XPS spectra of Co 2p, S 2p and C 1s in Co_9S_8/2CNTs sample (d)

D-band and G-band intensities (I_D/I_G) was 1.16:1, indicating the formation of abundant defect structures in the CNTs; this demonstrated that the incorporation of CNTs could provide additional defect sites for NH_4^+ storage and further enhance the electrochemical properties of Co_9S_8/2CNTs microspheres. Some weak bands below 750 cm^{-1} were perfectly indexed to Co_9S_8 crystals.

The specific surface area and pore size distribution of the microspheres were determined by the N_2 adsorption−desorption method. The two microspheres both exhibited typical IV isotherms and H3-type hysteresis loops, indicating the presence of microporous and mesoporous structures in the two microspheres (Fig. 1(c)). The specific surface area of the Co_9S_8/2CNTs microspheres was calculated to be 40.72 m^2/g, which was significantly higher than that of Co_9S_8 (12.20 m^2/g). The pore size distribution curves (inset in Fig. 1(c)) also showed that Co_9S_8/2CNTs microspheres had more abundant micropores and a relatively narrow pore size distribution than Co_9S_8 microspheres, which could accelerate the ion transfer and reduce the volume change during the cycling processes to improve the electrochemical properties of the materials.

The elemental composition and surface chemical state of Co_9S_8/2CNTs microspheres were further determined by XPS methods (Fig. S1 in Supporting Information (SI)). The binding energies of Co $2p_{3/2}$ and Co $2p_{1/2}$ ranged from 778 to 786 eV and from 793 to 803 eV, respectively (Fig. 1(d)). The peaks centered at 784.4 and 800.4 eV were satellite peaks for Co $2p_{2/3}$ and Co $2p_{1/2}$, respectively. The binding energies at 780.2 and 796.9 eV could be attributed to Co^{2+}, while those at 778.3 and 794.1 eV belonged to Co^{3+} [30,31]. Furthermore, the S 2p XPS spectrum was fitted to three peaks, which could be attributed to S in Co_9S_8 (162 eV), C—S—C (163.5 eV) and SO_4^{2-} (167.6 eV). The presence of SO_4^{2-} should be related to the partial surface oxidation of the sample [32]. The high-resolution XPS spectrum of C 1s revealed two peaks at approximately 284.8 eV for C—C

bonds and 285.5 eV for C—S bonds [33]. The C—S peaks were ascribed to the single bond between Co_9S_8 and carbon, demonstrating that carbon nanotubes were tightly attached to Co_9S_8. The above results further elucidated the chemical composition of Co_9S_8/2CNTs microspheres, which was consistent with the XRD patterns and Raman spectrum analysis.

Figure 2 shows a schematic diagram of the Co_9S_8 crystal structure. The structure consisted of two polyhedra for CoS_6 octahedra and CoS_4 tetrahedra, where each CoS_6 octahedron shared its six angles with 24 CoS_4 tetrahedra. Nine cobalt atoms in each formula occupied two Witkoff positions, CoI (4b) and CoII (32f), and eight sulfur atoms occupied two different Witkoff positions, SI (8c) and SII (24e). CoI coordination was formed from six SI atoms to form the CoS_6 octahedron, and CoII coordination was composed of one SII and three SI atoms to form the CoS_4 twisted tetrahedron [34].

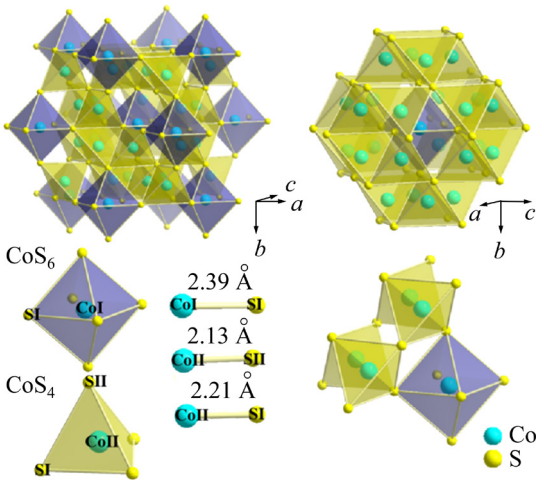

Fig. 2 Crystal structure and its partial enlargement

3.2 Morphology and microstructure

Figure 3 shows SEM and TEM images, and EDS mappings of Co_9S_8 and Co_9S_8/2CNTs microspheres. The inhomogeneous clustered microspheres could be distinguished from Figs. 3(a, b). The typical high-resolution transmission electron microscopy (HRTEM) images exhibited the single-crystal of Co_9S_8 microspheres with *d* spacings of 2.64 Å and 2.54 Å (Figs. 3(c, d)), corresponding to the (400) and (004) crystal planes, respectively. The corresponding Fourier transforms (FFTs) of the

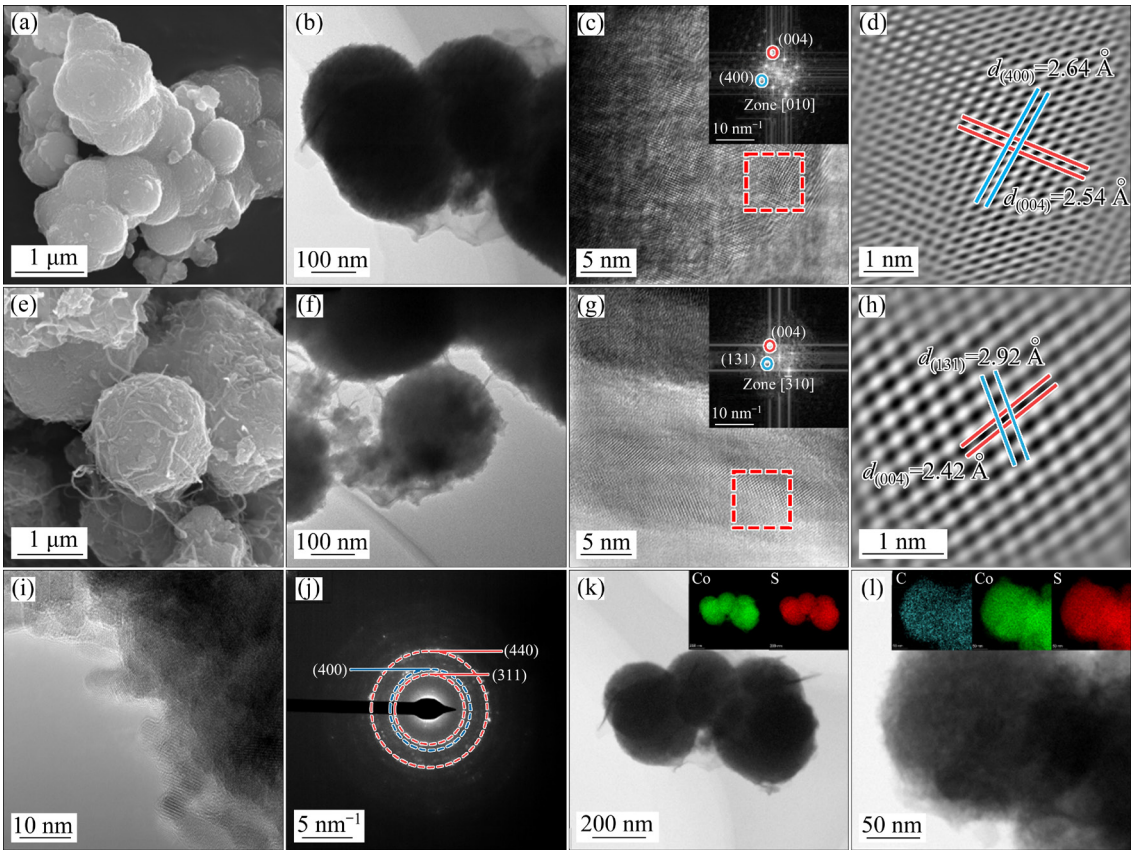

Fig. 3 SEM (a) and TEM (b−d) images of Co_9S_8, SEM (e) and TEM (f−i) images of Co_9S_8/2CNTs, selected area electron diffraction (SAED) diagram of Co_9S_8/2CNTs (j), and EDS mappings of Co_9S_8 (k) and Co_9S_8/2CNTs (l)

selected regions could be identified as cubic symmetric structures (inserted in Fig. 3(c)), which was in good agreement with the Co_9S_8 spatial structure (Fig. 2). For the Co_9S_8/2CNTs micro-spheres, the uniform and disperse microspheres were related to the CNTs (Figs. 3(e, f)). The HRTEM observations for the Co_9S_8/2CNTs microspheres (Figs. 3(g, h)) revealed crystal spacings of 2.92 nm and 2.42 nm, corresponding to (131) and (004) crystal planes, which were evidenced by the inserted FFTs (Fig. 3(g)). The three typical diffraction rings (Fig. 3(j)) could be attributed to (311), (400) and (440) planes of the Co_9S_8 phase (PDF# 65-1765). The EDS mapping images (Figs. 3(k, l)) for the Co_9S_8 and Co_9S_8/2CNTs microspheres confirmed the perfect overlap of Co and S but a slight extension of C due to the CNT combinations. The introduction of CNTs could inhibit the aggregation of active particles, alleviate electrode expansion to improve the structural stability during the cycling processes and enhance the electrical conductivity to increase the rate capability.

3.3 Electrochemical performance

The electrochemical performances of the Co_9S_8 and Co_9S_8/2CNTs microspheres were evaluated. Figures 4(a, b) display the typical charge−discharge curves of the Co_9S_8 and Co_9S_8/2CNTs microsphere electrodes at a current density of 0.1 A/g. The initial charge/discharge specific capacities were 186.4 and 113.2 mA·h/g for the Co_9S_8/2CNTs microspheres and 195.8 and 112.5 mA·h/g for the Co_9S_8 microspheres. The poor coulombic efficiency indicated irreversible reactions in the initial ammonization and deammonization processes. Although the Co_9S_8 and Co_9S_8/2CNTs microspheres exhibited almost identical discharge capacities in the initial cycle, they emerged with completely different capacity trends in the subsequent cycles. The Co_9S_8 microspheres suffered a continuous capacity decay with 95.3% capacity retention (107.2 mA·h/g) after 50 cycles. However, the discharge capacity for the Co_9S_8/2CNTs micro-spheres exhibited an evident increase at the second cycle followed by a sustained rise to 142.5 mA·h/g.

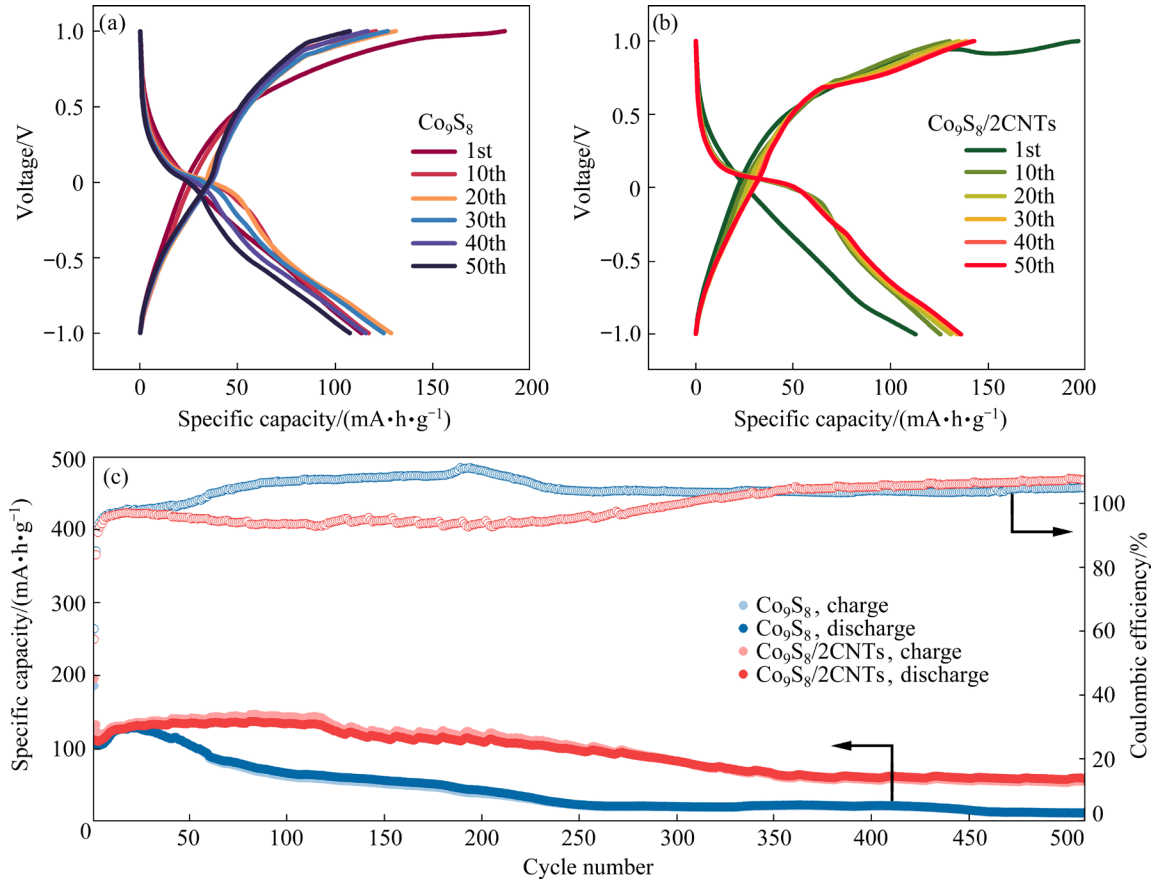

Fig. 4 Electrochemical performance of Co_9S_8/2CNTs cathode in voltage window from −1 to 1 V: (a) Charge–discharge curves of Co_9S_8 at 0.1 A/g; (b) Charge–discharge curves of Co_9S_8/2CNTs at 0.1 A/g; (c) Cyclic performance of Co_9S_8 and Co_9S_8/2CNTs at 0.1 A/g for 500 cycles

Compared with the Co_9S_8 microspheres, the Co_9S_8/2CNTs microspheres had significantly improved cycling stability after 500 cycles at a current density of 0.1 A/g (Fig. 4(c)). The Co_9S_8/2CNTs microspheres revealed a discharge capacity of 60 mA·h/g at the 500th cycle, which was markedly higher than that of the Co_9S_8 microspheres (13 mA·h/g). This result confirmed that the addition of CNTs could reduce the dissolution of Co_9S_8 polysulfides in the aqueous electrolyte, effectively buffering the large volume change of the Co_9S_8 microspheres during the discharge/charge processes [33,35]. The rate capabilities of Co_9S_8/2CNTs microspheres were investigated by changing the current density from 0.1 to 10.0 A/g (Fig. 5(a)). The Co_9S_8/2CNTs microspheres obtained an evidently higher capacity than the Co_9S_8 microspheres at any current density. The capacities for the Co_9S_8/2CNTs microspheres varied from 112 to 66 mA·h/g as the current densities increased from 0.1 to 10.0 A/g. When the current density was restored to 0.1 A/g, the capacity of Co_9S_8/2CNTs microspheres could recover back to 110 mA·h/g, indicating a good rate performance.

Figure 5(b) depicts the CV curves of the Co_9S_8/2CNTs microspheres in the voltage window between −0.5 and 1.2 V at different scanning rates from 0.4 to 1.0 mV/s. The two pairs of redox peaks could be obviously observed on the Co_9S_8/2CNTs microspheres, which was similar to the results of Co_9S_8 in lithium-ion batteries [25], indicating that the Co_9S_8/2CNTs microspheres manifested NH_4^+ energy storage. In the cathodic scanning, there were two reduction peaks at −0.4 and 0 V, which were related to NH_4^+ insertion in the Co_9S_8 host. In the anodic scanning, the oxidation peaks at 0.3 and 0.85 V approximately were attributed to NH_4^+ extraction in the Co_9S_8 host [36]. The totally stored charges were derived from the capacitive processes, including pseudocapacitors, double layer

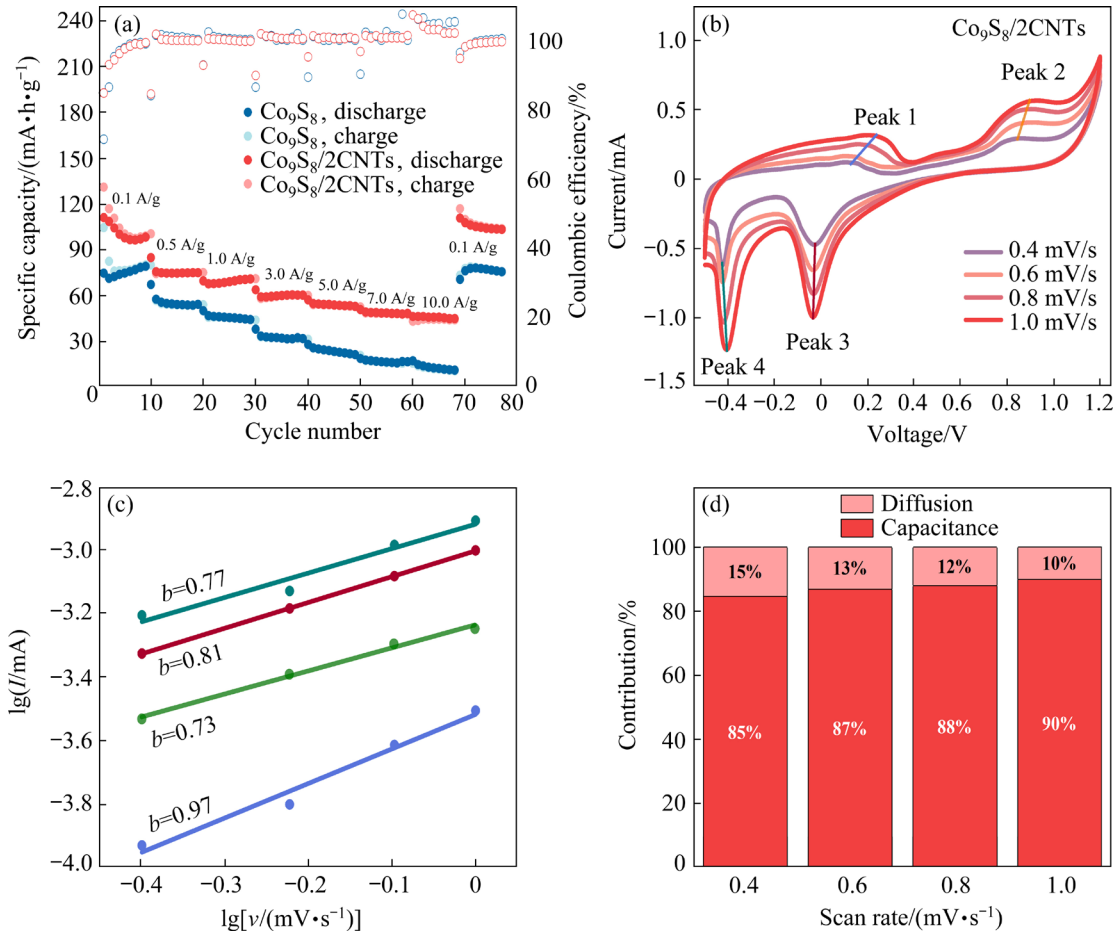

Fig. 5 Rate performances of Co_9S_8 and Co_9S_8/2CNTs at 0.1−10 A/g (a); CV curves at different scan rates (b) and corresponding lg I vs lg v plots of redox peaks (c) of Co_9S_8/2CNTs in Fig. 5(b); Diffusion/capacitance contributions at different scanning rates of Co_9S_8/2CNTs (d)

capacitors, capacitor contributions and diffusion-controlled Faraday intercalation processes. Generally, the measured peak current (I) in the CV curve and the corresponding scan rate (v) followed Eq. (1) [37]:

$$I=av^b \quad (1)$$

This can also be expressed as

$$\lg I=\lg a+b\lg v \quad (2)$$

where a and b are adjustable parameters. The b values of 0.5 and 1.0 were considered to be diffusion-controlled and capacitance-controlled processes, respectively. The calculated b values for the two pairs of redox peaks were 0.97, 0.73, 0.81 and 0.77 (Fig. 5(c)), indicating the combination of capacitance-controlled and diffusion-controlled behaviors.

In addition, diffusion/capacitance contribution at different scan rates could be calculated by Eq. (3):

$$I=k_1v+k_2v^{1/2} \quad (3)$$

where k_1v and $k_2v^{1/2}$ denote the capacitance and diffusion contributions, respectively. Therefore, the capacitive contributions could be calculated as 85%, 87%, 88% and 90% at scan rates of 0.4, 0.6, 0.8 and 1.0 mV/s (Fig. 5(d)), respectively, and only minor diffusion-controlled behaviors could be obtained.

3.4 Reaction mechanism

To reveal the structural evolution and chemical state changes of Co_9S_8 during NH_4^+ intercalation/deintercalation processes, XRD, FT-IR and XPS spectra at different states were recorded (Reference supporting information for equipment used for material characterization). During the first charge process (a−b in Fig. 6(a)), a new diffraction peak corresponding to $CoSO_4·6H_2O$ (PDF# 16-0304) appeared in the XRD spectra, indicating partly oxidized Co_9S_8. After the discharge to −1 V (Point e in Fig. 6(a)), the newly generated $CoSO_4·6H_2O$ returned to Co_9S_8 (Figs. 6(a, b)). From the magnified diffraction peaks (Fig. 6(b)), the (311) diffraction peaks shifted to low angles upon discharging and recovered the original position upon charging, indicating Co_9S_8 lattice expansion and shrinkage [38]. The highly reversible structural evolution of the Co_9S_8/2CNTs microspheres during

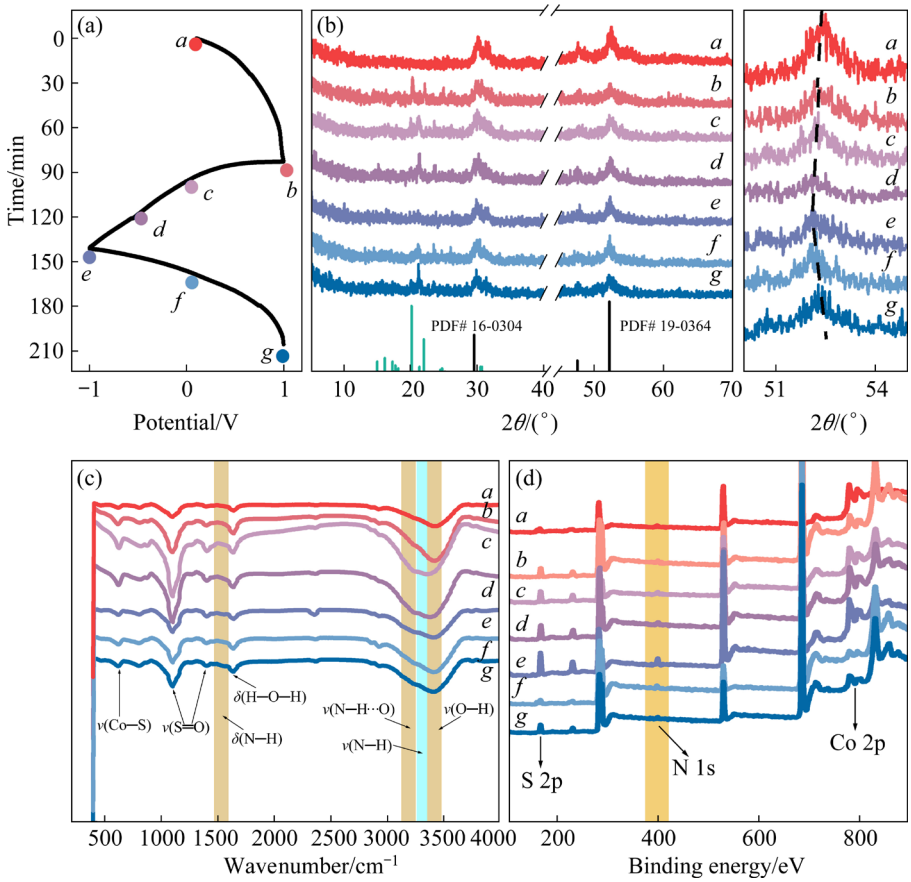

Fig. 6 Spectroscopic analysis of electrochemical reaction mechanism of Co_9S_8/2CNTs electrode: (a) Charge–discharge curve; (b) XRD patterns; (c) FT-IR characterization; (d) XPS spectra

the charge/discharge processes was the intrinsic manifestation of the excellent cycling stability.

The bonding chemistry between NH_4^+ and the host materials was investigated by FT-IR and XPS measurements (Figs. 6(c, d)). The peaks at 3422 and 1629 cm^{-1} were assigned to the stretching and bending vibrations of the O—H bond of chemisorbed water. The absorption peaks located at 1404 and 3145 cm^{-1} were credited with the bending and stretching vibrations of N—H [39,40]. The two peaks gradually increased upon discharging and recovered upon charging, indicating NH_4^+ intercalation/deintercalation. The peaks at 1093 and 1394 cm^{-1} were attributed to the symmetric and asymmetric vibrations of the S═O bond. The variation in the peaks demonstrated partial oxidation of Co_9S_8 in the charge processes and incomplete reduction of $CoSO_4·H_2O$ in the discharge processes. Meanwhile, the N—H···O hydrogen bond signal was observed near 3220 cm^{-1}, indicating the formation of hydrogen bonds between the inserted NH_4^+ and the oxidized Co_9S_8. After charging (*e*–*g* in Fig. 6(a)), the wide peak near 3220 cm^{-1} disappeared, indicating that the insertion/extraction of NH_4^+ ions in the Co_9S_8/2CNTs host was related to the oxidation/reduction of Co_9S_8 and building/breaking of hydrogen bonds [20,41,42]. This was also supported in the XPS survey spectra (Figs. 6(d) and 7(c)). The N 1s peak increased with NH_4^+ intercalation, and the XPS spectrum of N 1s moved to a higher binding direction, while the charge process was reversed, further indicating the interaction between NH_4^+ and the matrix material (Figs. 6(d) and 7(b)).

The S 2p XPS spectrum of Fig. 7(a) was fitted to three peaks from S in Co_9S_8 (162 eV), C—S—C (163.5 eV), and SO_4^{2-} (167.6 eV). The presence of SO_4^{2-} in the original electrode plate (Point *a* in Fig. 6(a)) should be related to the partial oxidation of the sample. After the first charge (Point *b* in Fig. 6(a)), the binding energy of SO_4^{2-} increased significantly, indicating formation of $CoSO_4·6H_2O$, which partially recovered upon discharging (Point *e* in Fig. 6(a)). From the N 1s spectra (Fig. 7(b)), peak states of —N—H—(NH_3) and —N+H—(NH_4^+) were obviously found, originating from two different states of NH_4^+ ions. Compared with the pristine state and the charged state, the ratio of —N—H—/—N+H— was significantly increased, demonstrating that more intercalated NH_4^+ ions existed in the form of NH_3. The N atom at 398.9 eV was ascribed to the C—N bond, which could originate from the interaction between the carbon nanotubes and the intercalated NH_4^+ ions [43,44].

The Co 2p spectrum (Fig. 7(c)) consisted of two spin-orbit doublets characterized by Co^{3+} (778.3, 794.1 eV) and Co^{2+} (780.2, 796.9 eV) and two shaking satellites [30,31]. Compared with State *b* (1.26:1), the ratio of Co^{3+}/Co^{2+} calculated by the corresponding integral peak area in the complete discharge state was 0.44:1. Owing to the embedding

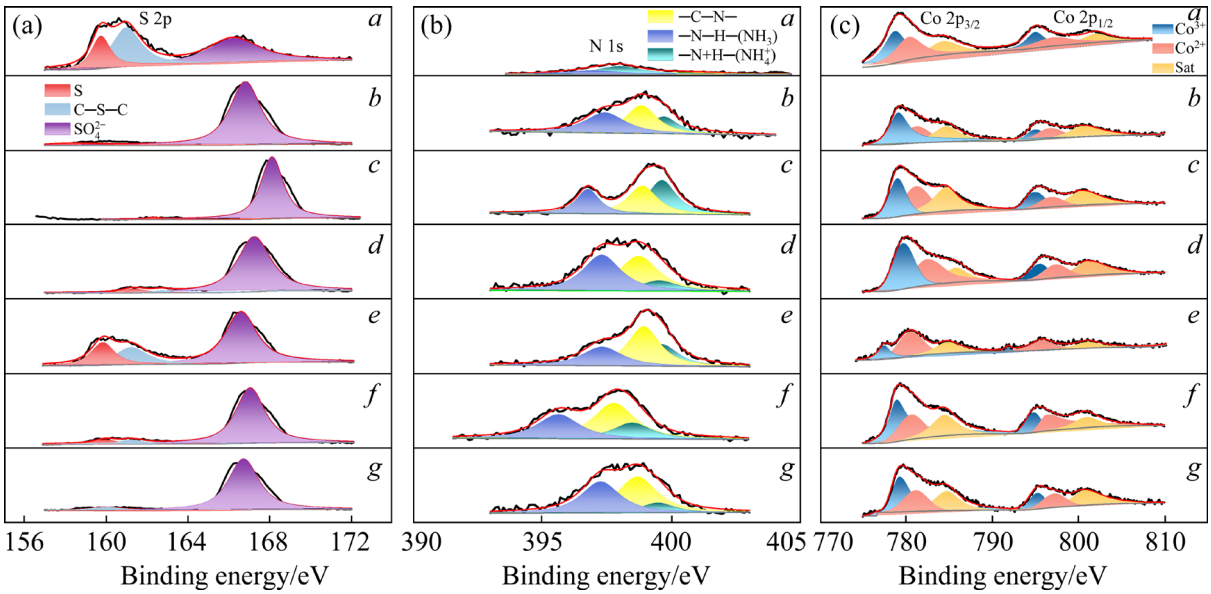

Fig. 7 High-resolution spectra of S 2p (a), N 1s (b) and Co 2p (c) corresponding to Co_9S_8/2CNTs circulating at different potentials during charge−discharge processes (*a*–*g* corresponding to Points *a*–*g* in Fig. 6(a))

of NH_4^+, the content of Co^{3+} decreased, while the content of Co^{2+} increased significantly. When charged to 0.3 V (Point *f*), the ratio of Co^{3+}/Co^{2+} increased to 1.17:1 due to NH_4^+ extraction. After being fully charged, the Co^{3+}/Co^{2+} ratio recovered to 1.23:1. The reversible charge transfer reaction showed that Co_9S_8/2CNTs was suitable electrode material for NH_4^+ accommodation; in terms of reaction chemistry, this could be attributed to the unusual hydrogen bonding interaction between NH_4^+ and the material, which contributed to the ultrafast storage kinetics of NH_4^+ [21,23,45,46].

3.5 Kinetic analysis

The aqueous ammonium-ion batteries assembled with Co_9S_8/2CNTs microspheres as the cathode and active carbon as the anode were evaluated under a practical operating voltage of 0.01−1.00 V. The CV curves presented a pair of distinct redox peaks (Fig. S2 in SI), indicating that NH_4^+ ions could be reversibly inserted/extracted from Co_9S_8/2CNTs microspheres. From the second scan, the CV curves could exactly overlap, suggesting the good cycling ability of Co_9S_8/2CNTs microspheres. The galvanostatic charge–discharge curves of the Co_9S_8/2CNTs microspheres (Fig. S3 in SI) exhibited a pair of voltage plateaus in the initial charge and discharge cycle, indicating that NH_4^+ was reversibly inserted/extracted from the Co_9S_8/2CNTs microspheres, which was consistent with the CV results. For the next 10−60 cycles, the voltage platform remained in the same position. The Co_9S_8/2CNTs microspheres (Fig. 8) provided 60, 46, 39, 32, 28, 27 and 25 mA·h/g at current densities of 0.1, 0.5, 1.0, 3.0, 5.0, 7.0 and 10.0 A/g, respectively, suggesting a good rate performance. Impressively, when the current density was continuously decreased to 0.1 A/g, it still provided a discharge specific capacity of 57 mA·h/g with a ratio of 95%. Table S1 in SI demonstrates the performance of various NH_4^+ cathode host materials, and it can be inferred that the specific capacity of Co_9S_8 as an ammonium ion battery cathode material is superior to some of the reported ammonium ion battery materials, such as NiHCF (38 mA·h/g at 0.5 A/g) and NiAPW (51.3 mA·h/g at 0.3 A/g), and is only followed by some vanadium- and manganese-based composite cathode materials.

The evolution of charge transfer during cycling was investigated by electrochemical impedance spectroscopy (EIS) and galvanostatic intermittent titration technique (GITT). All Nyquist plots consisted of a semicircle in the high-frequency region and a linear part in the low-frequency region, where the semicircle region represented the charge transfer impedance (R_{ct}), and the intercept of the real axis in the high-frequency range corresponded to the ohmic resistance (R_s). In the EIS plot measured before cycling (Fig. 9(a)), the R_{ct} of the Co_9S_8/2CNTs microspheres was smaller than that of the Co_9S_8 microspheres. Figures 9(b, c) illustrate the change in R_{ct} and R_s (related to byproducts) as a potential function. Upon charging, an increased R_s was observed due to the formation of $CoSO_4·6H_2O$ with poor conductivity [47]. The R_s values could recover upon discharging due to the reversible reduction of $CoSO_4·6H_2O$. Meanwhile, R_{ct} showed a gradually decreasing trend in the discharge process, and the impedance increased after decreasing to platform *b*−*c* in Fig. 6(a), which was caused by the volume expansion of the Co_9S_8/2CNTs microspheres. In the subsequent charging to plateaus *e*−*f* in Fig. 6(a), R_{ct} and R_s reached the bottom. The charge transfer resistance of the Co_9S_8/2CNTs microspheres was 4.6 Ω before the charge and discharge processes and 2.5 and 0.3 Ω after the discharge and charge processes, indicating that the reduction in charge transfer resistance was related to activation processes [48,49].

The diffusion coefficient of ammonium ions can be derived using Eq. (4) (please refer to the supporting information for details) [50]:

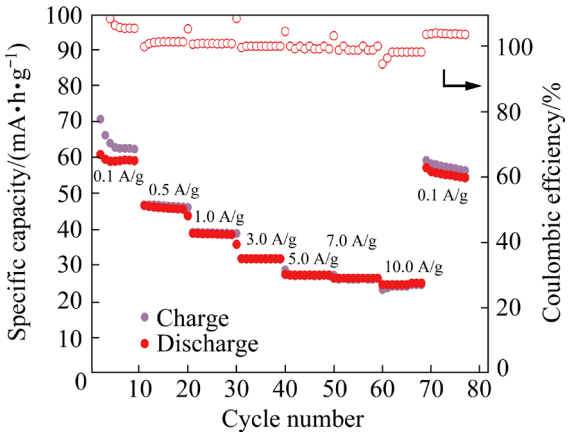

Fig. 8 Electrochemical performance of Co_9S_8/2CNTs cathode in voltage window of 0.01−1.00 V and rate performance of Co_9S_8/2CNTs cathode at 0.1−10.0 A/g

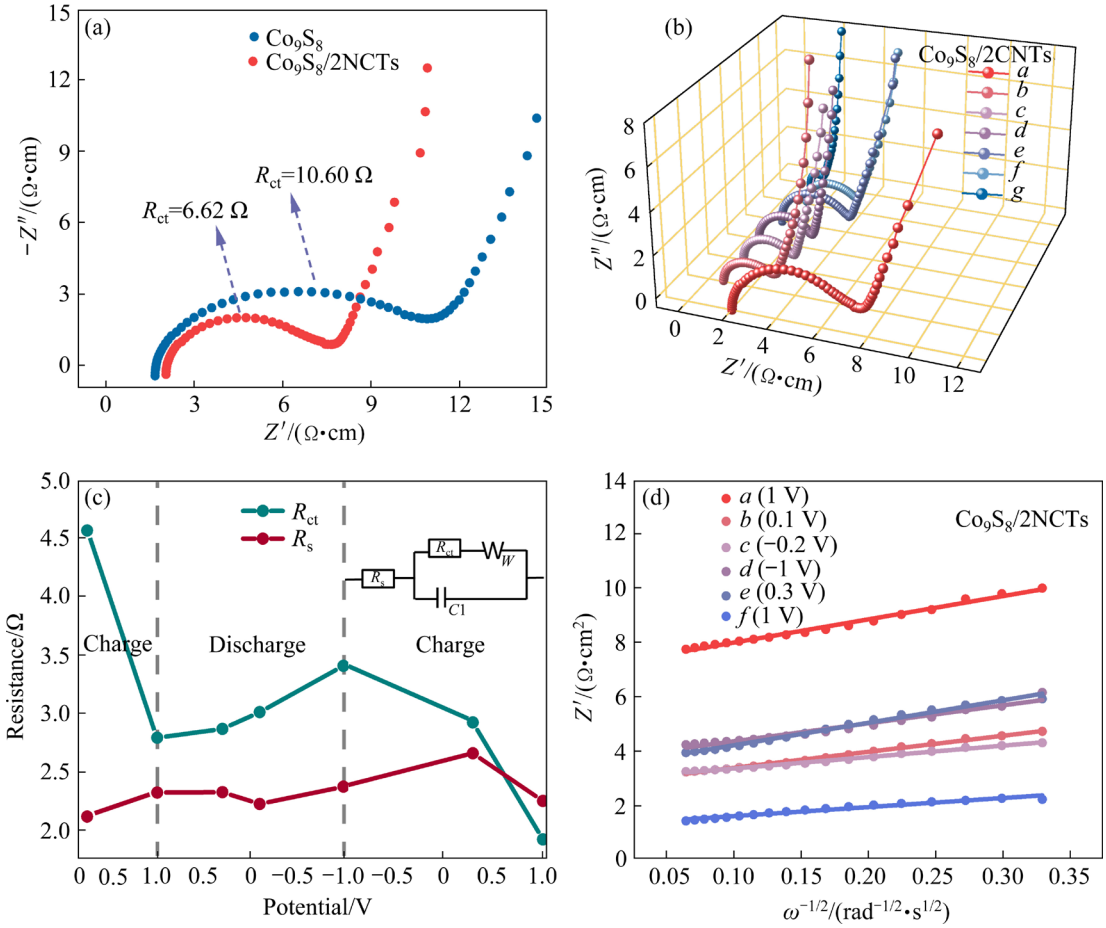

Fig. 9 (a) Precycle Nyquist plots of Co_9S_8 and Co_9S_8/2CNTs cathodes; (b) Nyquist plots obtained at various potentials during the 1st cycle of Co_9S_8/2CNTs cathode; (c) R_s and R_{ct} at different potentials (inset shows the equivalent circuit for fitting the EIS curve) of Co_9S_8/2CNTs cathode; (d) Corresponding linear curves of Z' vs $\omega^{-1/2}$ in low-frequency region of Co_9S_8/2CNTs cathode

$$D=\frac{R^2T^2}{2A^2n^4F^4C^2\sigma^2} \tag{4}$$

The ammonium-ion diffusion coefficients (denoted by $D(NH_4^+)$) in the Co_9S_8 and Co_9S_8/2CNTs microspheres were calculated to be as high as 2.58×10^{-10} and 8.25×10^{-10} cm^2/s, respectively. This result demonstrated that the ammonium-ion reaction kinetics of Co_9S_8/2CNTs microspheres was remarkably fast. In addition, the relationships between Z' and the inverse square root of the angular frequency ($\omega^{-1/2}$) are shown in Fig. 9(d). According to the slope of the fitted Z'–$\omega^{-1/2}$ curve, the Warburg coefficients during the first cycle were 8.5, 6.2, 5.9, 4.2, 6.6, 8.3 and 3.3. The ion diffusion coefficients were inversely proportional to the slope of the fitted curve of Z'–$\omega^{-1/2}$, which was consistent with the available literature. During the first cycle from the Co_9S_8/2CNTs microspheres discharged to platform c–d in Fig. 6(a), $D(NH_4^+)$ increased, and when discharged to −1 V (Point e in Fig. 6(a)), $D(NH_4^+)$ decreased to 1.37×10^{-8} cm^2/s, and when charged to 1 V (Point g in Fig. 6(a)), $D(NH_4^+)$ increased to the maximum value of 5.47×10^{-8} cm^2/s. These results demonstrated the improved capacity and rate performance.

The ammonium-ion diffusion coefficients were also measured by the GITT technique (Fig. 10). It was calculated based on the following Eq. (5) (refer to supporting information for details) [51]:

$$D=\frac{4}{\pi\tau}\left(\frac{m_BV_m}{M_BS}\right)^2\left(\frac{\Delta E_s}{\Delta E_\tau}\right)^2 \tag{5}$$

The NH_4^+ diffusion coefficients in the Co_9S_8/2CNTs microspheres were calculated to be approximately 10^{-7}–10^{-9} cm^{-2}/s, and the results were in good agreement with the EIS results. A

relatively stable trend of $D(NH_4^+)$ could be observed throughout the charge-discharge testing processes, indicating the rapid and stable diffusion behavior of NH_4^+ ions during insertion/extraction from the Co_9S_8 host.

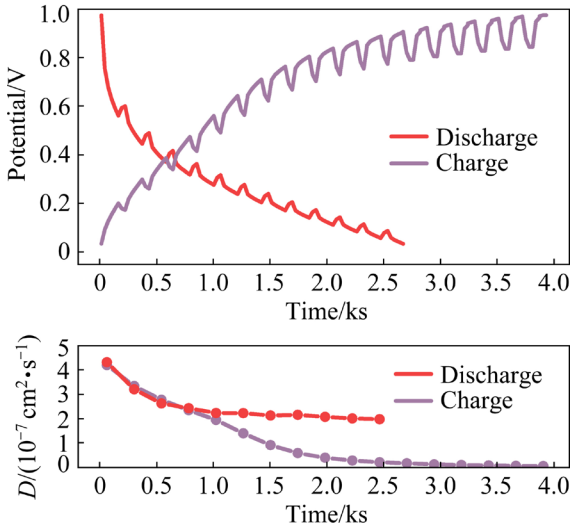

Fig. 10 Charge–discharge curves of Co_9S_8/2CNTs cathode and corresponding NH_4^+ diffusion coefficient (D)

4 Conclusions

(1) CNTs introduction could improve the dispersion of the material, widen the lattice spacing and increase the specific surface area of material; moreover, it could improve the electron transfer and restrain the volume variation and dissolution of polysulfides during the cycling processes.

(2) The Co_9S_8/2CNTs microspheres were revealed to be favorable to the rapid penetration of electrolyte and the short diffusion distance of ammonium ions.

(3) The reversible phase transition between Co_9S_8 and $CoSO_4·6H_2O$ was found during the charge/discharge process. Moreover, the highly reversible insertion/extraction of NH_4^+ ions in the Co_9S_8 host was accompanied by the building/breaking of intermolecular hydrogen bonds.

(4) The Co_9S_8/2CNTs microspheres were considered potential cathodes for the aqueous ammonium-ion batteries.

Acknowledgments

This work was supported by the National Natural Science Foundation of China (Nos. 52171200, 51972108) and Changsha Special Project, China (No. kh2301006).

Supporting Information

Supporting Information in this paper can be found at: http://tnmsc.csu.edu.cn/download/17-p3452-2023-0669-Supporting_Information.pdf.

References

[1] SUN Ze-hang, LIU Yang, YE Wei-bin, ZHANG Jin-yang, WANG Yu-yan, LIN Yue, HOU Lin-rui, WANG Ming-sheng, YUAN Chang-zhou. Unveiling intrinsic potassium storage behaviors of hierarchical nano Bi@N-doped carbon nanocages framework via in situ characterizations [J]. Angewandte Chemie International Edition, 2021, 60: 7180−7187.

[2] QIN Mu-lan, YIN Chang-yu, XU Wen, LIU Yang, WEN Jun-hao, SHEN Bin, WANG Wei-gang, LIU Wan-min. Facile synthesis of high capacity P2-type $Na_{2/3}Fe_{1/2}Mn_{1/2}O_2$ cathode material for sodium-ion batteries [J]. Transactions of Nonferrous Metals Society of China, 2021, 31: 2074−2080.

[3] DENG Wei-na, XU Yi-xue, ZHANG Xiang-chao, LI Cheng-yong, LIU Ying-xin, XIANG Kai-xiong, CHEN Han. $(NH_4)_2Co_2V_{10}O_{28}·16H_2O/(NH_4)_2V_{10}O_{25}·8H_2O$ hetero-structure as cathode for high-performance aqueous Zn-ion batteries [J]. Journal of Alloys and Compounds, 2022, 903: 163824.

[4] LIU Zhen, HE Han-bing, LUO Ze-xiang, WANG Xiao-feng, ZENG Jing. 3D printing of customized MnO_2 cathode for aqueous zinc-ion batteries [J]. Transactions of Nonferrous Metals Society of China, 2023, 33: 1193−1204.

[5] WEI Lu-yao, LIAN Ru-qian, WANG Da-shuai, ZHAO Ying-ying, YANG Di, ZHAO Hai-nan, WANG Yi-zhan, CHEN Gang, WEI Ying-jin. Magnesium ion storage properties in a layered $(NH_4)_2V_6O_{16}·1.5H_2O$ nanobelt cathode material activated by lattice water [J]. ACS Applied Materials & Interfaces, 2021, 13: 30625−30632.

[6] PONROUCH A, FRONTERA C, BARDÉ F, PALACÍN M R. Towards a calcium-based rechargeable battery [J]. Nature Materials, 2016, 15: 169−172.

[7] WANG Hua-li, BAI Ying, CHEN Shi, LUO Xiang-yi, WU Chuan, WU Feng, LU Jun, AMINE K. Binder-free V_2O_5 cathode for greener rechargeable aluminum battery [J]. ACS Applied Materials & Interfaces, 2015, 7: 80−84.

[8] XU Jia-xi, LIU Yi-wen, XU Chi-wei, LI Jing, YANG Zheng-wei, YAN Hui-hui, YU Hao-xiang, YAN Lei, ZHANG Li-yuan, SHU Jie. Aqueous non-metallic ion batteries: Materials, mechanisms and design strategies [J]. Coordination Chemistry Reviews, 2023, 474: 214867.

[9] WU Xian-yong, QI Yi-tong, HONG J J, LI Zhi-fei, HERNANDEZ A S, JI Xiu-lei. Rocking-chair ammonium-ion battery: A highly reversible aqueous energy storage system [J]. Angewandte Chemie International Edition, 2017, 56: 13026−13030.

[10] SU Zhen, CHEN Jun-bo, STANSBY J, JIA Chen, ZHAO Ting-wen, TANG Jia-qi, FANG Yu, RAWAL A, HO Jun-ming, ZHAO Chuan. Hydrogen-bond disrupting electrolytes for fast and stable proton batteries [J]. Small, 2022, 18: 2201449.

[11] SU Zhen, TANG Jia-qi, CHEN Jun-bo, GUO Hao-cheng,

WU Si-cheng, YIN Song-yan, ZHAO Ting-wen, JIA Chen, MEYER Quen-tin, RAWAL A, HO Jun-ming, FANG Yu, ZHAO Chuan. Co-insertion of water with protons into organic electrodes enables high-rate and high-capacity proton batteries [J]. Small Structures, 2023, 4: 2200257.

[12] SIDEY V. On the effective ionic radii for ammonium [J]. Acta Crystallographica Section B, 2016, 72: 626−633.

[13] CHAO Dong-liang, FAN Hong-Jin. Intercalation pseudo-capacitive behavior powers aqueous batteries [J]. Chem, 2019, 5: 1359−1361.

[14] ZHENG Run-tian, LI Yu-hang, YU Hao-xiang, ZHANG Xi-kun, YANG Ding, YAN Lei, LI Yu, SHU Jie, SU Bao-lian. Ammonium ion batteries: Material, electrochemistry and strategy [J]. Angewandte Chemie International Edition, 2023, 62: e202301629.

[15] WESSELLS C D, PEDDADA S V, MCDOWELL M T, HUGGINS R A, CUI Yi. The effect of insertion species on nanostructured open framework hexacyanoferrate battery electrodes [J]. Journal of the Electrochemical Society, 2011, 159: A98.

[16] XIA Mao-ting, ZHANG Xi-kun, YU Hao-xiang, YANG Zheng-wei, CHEN Shi, ZHANG Li-yuan, SHUI Miao, XIE Ying, SHU Jie. Hydrogen bond chemistry in $Fe_4[Fe(CN)_6]_3$ host for aqueous NH_4^+ batteries [J]. Chemical Engineering Journal, 2021, 421: 127759.

[17] KUCHENA S F, WANG Ying. Superior polyaniline cathode material with enhanced capacity for ammonium ion storage [J]. ACS Applied Energy Materials, 2020, 3: 11690−11698.

[18] ZHANG Ya-di, AN Yu-feng, YIN Bo, JIANG Jiang-min, DONG Sheng-yang, DOU Hui, ZHANG Xiao-gang. A novel aqueous ammonium dual-ion battery based on organic polymers [J]. Journal of Materials Chemistry A, 2019, 7: 11314−11320.

[19] DONG Sheng-yang, SHIN W, JIANG Heng, WU Xian-yong, LI Zhi-fei, HOLOUBEK J, STICKLE W F, KEY B, LIU Cong, LU Jun, GREANEY P A, ZHANG Xiao-gang, JI Xiu-lei. Ultra-fast NH_4^+ storage: Strong H bonding between NH_4^+ and Bi-layered V_2O_5 [J]. Chem, 2019, 5: 1537−1551.

[20] SONG Yu, PAN Qing, LV Hui-zhen, YANG Duo, QIN Zeng-ming, ZHANG Ming-yue, SUN Xiao-qi, LIU Xiao-xia. Ammonium-ion storage using electrodeposited manganese oxides [J]. Angewandte Chemie International Edition, 2021, 60: 5718−5722.

[21] HOLOUBEK J J, JIANG Heng, LEONARD D, QI Yi-tong, BUSTAMANTE G C, JI Xiu-lei. Amorphous titanic acid electrode: its electrochemical storage of ammonium in a new water-in-salt electrolyte [J]. Chemical Communications, 2018, 54: 9805−9808.

[22] LI Hui, YANG Jie, CHENG Jian-li, HE Tao, WANG Bin. Flexible aqueous ammonium-ion full cell with high rate capability and long cycle life [J]. Nano Energy, 2020, 68: 104369.

[23] LIANG Guo-jin, WANG Yan-lei, HUANG Zhao-dong, MO Fu-nian, LI Xin-liang, YANG Qi, WANG Dong-hong, LI Hong-fei, CHEN Shi-mou, ZHI Chun-yi. Initiating hexagonal MoO_3 for superb-stable and fast NH_4^+ storage based on hydrogen bond chemistry [J]. Advanced Materials, 2020, 32: 1907802.

[24] WEN Xiao-yu, LUO Jin-hua, XIANG Kai-xiong, ZHOU Wei, ZHANG Chang-fan, CHEN Han. High-performance monoclinic WO_3 nanospheres with the novel NH_4^+ diffusion behaviors for aqueous ammonium-ion batteries [J]. Chemical Engineering Journal, 2023, 458: 141381.

[25] ZENG Pei-yuan, LI Jian-wen, YE Ming, ZHUO Kai-feng, FANG Zhen. In situ formation of Co9S8/N-C hollow nanospheres by pyrolysis and sulfurization of ZIF-67 for high-performance lithium-ion batteries [J]. Chemistry−A European Journal, 2017, 23: 9517−9524.

[26] DENG Wei-na, LI Yan-hua, XU Di-fa, ZHOU Wei, XIANG Kai-xiong, CHEN Han. Three-dimensional hierarchically porous nitrogen-doped carbon from water hyacinth as selenium host for high-performance lithium−selenium batteries [J]. Rare Metals, 2022, 41: 3432−3445.

[27] HUANG Tao, DING Jia-fen, LIU Zi-rui, ZHANG Rui, ZHANG Bo-Lei, XIONG Kai, ZHANG Long-zhou, WANG Chong, SHEN Shi-li, LI Cui-yu, YANG Peng, QIU Feng. Insight into the underlying competitive mechanism for the shift of the charge neutrality point in a trilayer-graphene field-effect transistor [J]. eScience, 2022, 2: 319−328.

[28] ZHOU Yong-sheng, ZHU Ying-chun, XU Bing-she, ZHANG Xue-ji, AL-GHANIM K A, MAHBOOB S. Cobalt sulfide confined in N-doped porous branched carbon nanotubes for lithium-ion batteries [J]. Nano−Micro Letters, 2019, 11: 29.

[29] LIU Yang, SUN Ze-hang, SUN Xuan, LIN Yue, TAN Ke, SUN Jin-feng, LIANG Long-wei, HOU Lin-rui, YUAN Chang-zhou. Construction of hierarchical nanotubes assembled from ultrathin V_3S_4@C nanosheets towards alkali-ion batteries with ion-dependent electrochemical mechanisms [J]. Angewandte Chemie International Edition, 2020, 59: 2473−2482.

[30] LI Jing-fa, XIONG Sheng-lin, LIU Yu-rong, JU Zhi-cheng, QIAN Yi-tai. High electrochemical performance of monodisperse $NiCo_2O_4$ mesoporous microspheres as an anode material for Li-ion batteries [J]. ACS Applied Materials & Interfaces, 2013, 5: 981−988.

[31] DOU Shuo, TAO Li, HUO Jia, WANG Shuang-yin, DAI Li-ming. Etched and doped Co_9S_8/graphene hybrid for oxygen electrocatalysis [J]. Energy & Environmental Science, 2016, 9: 1320−1326.

[32] PU Jun, WANG Zheng-hua, WU Kong-lin, YU Nan, SHENG En-hong. Co_9S_8 nanotube arrays supported on nickel foam for high-performance supercapacitors [J]. Physical Chemistry Chemical Physics, 2014, 16: 785−791.

[33] MUJTABA J, SUN Hong-yu, HUANG Guo-yong, ZHAO Yan-yan, ARANDIYAN H, SUN Guo-xing, XU Sheng-ming, ZHU Jing. Co_9S_8 nanoparticles encapsulated in nitrogen-doped mesoporous carbon networks with improved lithium storage properties [J]. RSC Advances, 2016, 6: 31775−31781.

[34] LIU Xu-dong, LIU Hua-tao, ZHAO Yan-ming, DONG You-zhong, FAN Qing-hua, KUANG Quan. Synthesis of the carbon-coated nanoparticle Co_9S_8 and its electrochemical performance as an anode material for sodium-ion batteries [J]. Langmuir, 2016, 32: 12593−12602.

[35] SHI Wen-hui, ZHU Ji-xin, RUI Xian-hong, CAO Xie-hong, CHEN C, ZHANG Hua, HNG Huey Hoon, YAN Qing-yu. Controlled synthesis of carbon-coated cobalt sulfide nanostructures in oil phase with enhanced Li storage performances [J]. ACS Applied Materials & Interfaces, 2012, 4: 2999−3006.

[36] LI Xiao-yan, LI Kai-kai, ZHU Si-cong, FAN Ke, LYU Lin-long, YAO Hai-min, LI Yi-yang, HU Jin-lian, HUANG Hai-tao, MAI Yiu-Wing, GOODENOUGH J B. Fiber-in-tube design of Co_9S_8−carbon/Co_9S_8: Enabling efficient sodium storage [J]. Angewandte Chemie International Edition, 2019, 58: 6239−6243.

[37] XING Jun-jie, FU Xiu-li, GUAN Shun-dong, ZHANG Yu, LEI Ming, PENG Zhi-jian. Novel K−V−Fe prussian blue analogues nanocubes for high-performance aqueous ammonium ion batteries [J]. Applied Surface Science, 2021, 543: 148843.

[38] ZHANG Xi-kun, XIA Mao-ting, LIU Ting-ting, PENG Na, YU Hao-xiang, ZHENG Run-tian, ZHANG Li-yuan, SHUI Miao, SHU Jie. Copper hexacyanoferrate as ultra-high rate host for aqueous ammonium ion storage [J]. Chemical Engineering Journal, 2021, 421: 127767.

[39] LIU Ya-ning, XU Mao-wen, SHEN Bo-lei, XIA Ze-min, LI Yuan, WU Yi, LI Qing. Facile synthesis of mesoporous $NH_4V_4O_{10}$ nanoflowers with high performance as cathode material for lithium battery [J]. Journal of Materials Science, 2018, 53: 2045−2053.

[40] ZHANG Xi-kun, XIA Mao-ting, YU Hao-xiang, ZHANG Jun-wei, YANG Zheng-wei, ZHANG Li-yuan, SHU Jie. Hydrogen bond-assisted ultra-stable and fast aqueous NH^{4+} storage [J]. Nano−Micro Letters, 2021, 13: 139.

[41] SHRIVASTAV V, SUNDRIYAL S, GOEL P, SHRIVASTAV V, TIWARI U K, DEEP A. ZIF-67 derived Co_3S_4 hollow microspheres and WS_2 nanorods as a hybrid electrode material for flexible 2 V solid-state supercapacitor [J]. Electrochimica Acta, 2020, 345: 136194.

[42] QIN Wei, HAN Lu, BI Hai, JIAN Jia-huang, WU Xiao-hong, GAO Peng. Hydrogen storage in a chemical bond stabilized Co_9S_8–graphene layered structure [J]. Nanoscale, 2015, 7: 20180−20187.

[43] MENG Xing, WANG Hai-ning, WANG Xiao-kun, DONG Long-zhang, ZOU Yan-hong. Cations mediating proton conductivity in an oxalate based microporous coordination polymer [J]. New Journal of Chemistry, 2019, 43: 24−27.

[44] SHI Xiao-hui, CHEN Li, LIU Bo-wen, LONG Jia-wei, XU Ying-jun, WANG Yu-zhong. Carbon fibers decorated by polyelectrolyte complexes toward their epoxy resin composites with high fire safety [J]. Chinese Journal of Polymer Science, 2018, 36: 1375−1384.

[45] TANG Xue-kun, HUANG Jing, FENG Qi-ming, LIU Kun, LUO Xian-ping, LI Zi-shun. Carbon sphere@Co_9S_8 yolk−shell structure with good morphology stability for improved lithium storage performance [J]. Nanotechnology, 2017, 28: 375402.

[46] CUI Wen-jing, ZHANG Si-meng, TIAN Ze-yu, LI Chen, WANG Yi-meng, YU Bo-rong, MA Yuan-yuan, HAN Zhan-gang. Hydrogen bond-mediated polyoxometalate-based metal-organic networks for efficient and selective oxidation of aryl alkenes to aldehydes [J]. Tungsten, 2022, 4(2): 109−120.

[47] WANG Yan-yi, YANG Ming, MA Ding-tao, CHEN Min-feng, CHEN Ji-zhang, HE Ting-shu, ZHANG Pei-xin. In-situ electrochemical etching of V_4AlC_3 MAX to V_2O_5/C composite as Zn-ion storage host [J]. Chemical Engineering Journal, 2023, 451: 138809.

[48] GENG Hong-bo, YANG Jun, DAI Zheng-fei, ZHANG Yu, ZHENG Yun, YU Hong, WANG Huan-wen, LUO Zhong-zhen, GUO Yuan-yuan, ZHANG Yu-fei, FAN Hao-sen, WU Xing-long, ZHENG Jun-wei, YANG Yong-gang, YAN Qing-yu, GU Hong-wei. Co_9S_8/MoS_2 yolk–shell spheres for advanced Li/Na storage [J]. Small, 2017, 13: 1603490.

[49] ZHANG Wan-yu, LU Ying, LI Zhou, WANG Yang, SUN Xiu-wei, WANG Qian, ZHANG Zhong, LIU Shu-xia. Incorporation of polyoxometalate-based acid–base pair into a sulfonated MIL-101 for achieving proton-conduction materials with high proton conductivity and high stability [J]. Tungsten, 2022, 4(2): 130−137.

[50] ZHANG S, DENG C, FU B L, YANG S Y, MA L. Doping effects of magnesium on the electrochemical performance of Li_2FeSiO_4 for lithium ion batteries [J]. Journal of Electroanalytical Chemistry, 2010, 644: 150−154.

[51] ZHANG Ning, JIA Ming, DONG Yang, WANG Yuan-yuan, XU Jian-zhong, LIU Yong-chang, JIAO Li-fang, CHENG Fan-gyi. Hydrated layered vanadium oxide as a highly reversible cathode for rechargeable aqueous zinc batteries [J]. Advanced Functional Materials, 2019, 29: 1807331.

含碳纳米管包覆 Co_9S_8 微球的高性能铵离子电池正极材料

黄玉柱[1,2]，幸 琳[1,2]，裴 双[1,2]，周 伟[2]，胡宇杰[1]，邓维娜[2]，陈 亮[2]，朱 海[2]，陈 晗[2]

1. 湖南工业大学 材料与先进制造学院，株洲 412007；
2. 长沙大学 材料与环境工程学院，长沙 410022

摘 要：构建 Co_9S_8/碳纳米管(Co_9S_8/2CNTs)涂层微球，并成功将其应用于水性铵离子电池。在 Co_9S_8 微球中引入碳纳米管可增加电子传导性，缩短 NH_4^+离子的扩散距离，并提高对循环过程中体积变化的缓冲能力。因此，Co_9S_8/2CNTs 微球在 0.1 A/g 条件下具有 112 mA·h/g 的可逆容量。此外，研究了 Co_9S_8/2CNTs 中伴随着可逆相变产物 $CoSO_4·6H_2O$ 的形成和分子间氢键的形成/断裂的铵离子储能机理。

关键词：硫化钴；碳纳米管；铵离子电池；复合微球；氢键

(Edited by Bing YANG)